

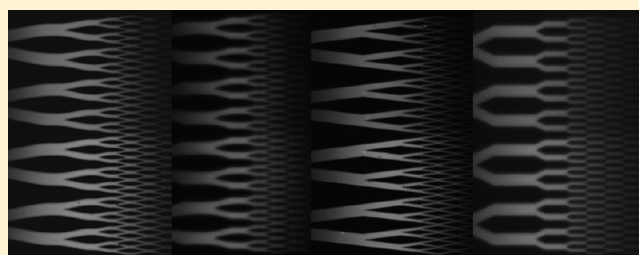
# Performance Evaluation of Different Design Alternatives for Microfabricated Nonporous Fused Silica Pillar Columns for Capillary Electrochromatography

Sertan Sukas,<sup>†</sup> Wim De Malsche,<sup>‡,†</sup> Gert Desmet,<sup>‡</sup> and Han J.G.E. Gardeniers<sup>\*,†</sup>

<sup>†</sup>Mesoscale Chemical Systems, MESA+ Institute for Nanotechnology, University of Twente, P.O. Box 217, 7500AE Enschede, The Netherlands

<sup>‡</sup>Department of Chemical Engineering, Vrije Universiteit Brussels, Pleinlaan 2, 1050 Brussels, Belgium

**ABSTRACT:** An experimental study comparing the performance of different designs for microfabricated column structures for microchip capillary electrochromatography is presented. The work is a follow-up to our previously published modeling and simulation study on the same topic. Experiments were performed using fused silica microchips with and without octadecyltrimethoxysilane coating for nonretained and retained modes of operation, respectively. Showing the same trends as the modeling results, the foil shape produces a significant decrease in plate height with an increase of around 15% in mobile phase velocity in nonretained measurements of Coumarin 480 (C480). Measured plate heights at 1 kV/cm applied electric field were 0.77, 1.33, and 1.42  $\mu\text{m}$  for foil, diamond, and hexagon, respectively. Chromatographic runs of C480 yielded minimal plate height values of 1.85 and 3.28  $\mu\text{m}$  for foil and diamond, respectively. The optimization of the shape and placement of the structures appeared to have a considerable impact on the achievable performance.



In 1998 Regnier and co-workers introduced the idea of using microfabricated column structures<sup>1</sup> for liquid chromatography (LC) as a promising concept with the potential of replacing packed column technology by microchips. Several follow-up studies of this work have since been published.<sup>2–11</sup> Regnier and his team published an experimental capillary electrochromatography (CEC) comparison of different geometries of their “collocated monolithic support structures” (COMOSS), namely, channel depths of 1.6–10  $\mu\text{m}$ , pillar gaps of 2–4  $\mu\text{m}$ , pillar shapes including diamonds with sides of 5–11  $\mu\text{m}$ , and their elongated and extended versions.<sup>3</sup> The application of microfabricated pillars for CEC has been continued by Kutter and co-workers during the past decade,<sup>4,5</sup> with a focus on fabrication methods and substrate materials, and on in-line optical detection. Desmet’s group published a series of theoretical and experimental papers discussing performance measures of microfabricated column structures, with a focus on high-performance liquid chromatography (HPLC) but including also some work on CEC.<sup>7–11</sup> Since the published work up to now has left the impression that the performance of CEC using COMOSS may still be improved, one reason being that micromachining technology has significantly advanced to a state where it is now possible to fabricate almost perfectly vertical structures in silicon and fused silica, we have continued the previous studies in order to find the ultimate performance of COMOSS for CEC. Our theoretical study in the field of CEC on the optimization of the shape and positioning of the microfabricated column structures coupled with retention modeling for solid pillars was

published in 2010.<sup>12</sup> A new geometry was introduced instead of using the basic geometrical shapes used by others, and its performance was compared with the ones from literature. In two-dimensional ideal conditions, the proposed foil shape yielded a moderate increase in performance (in terms of plate height) among the other alternatives. To complete the research on the performance of design alternatives for solid microfabricated fused silica pillar columns for CEC, in the present study, the validity of the earlier proposed definitions and boundary conditions will be experimentally evaluated.

## ■ EXPERIMENTAL SECTION

**Fabrication.** Being the most commonly used material for CEC applications both in conventional and microscale systems, fused silica was selected as a structural material because it is mechanically robust, optically transparent down to the UV regime, electrically stable, and durable in terms of surface properties, while commercial substrates are of very good optical quality with almost no inhomogeneity. Microchips were fabricated with a simple two-mask process as illustrated in Figure 1. First, a 1  $\mu\text{m}$  thick poly-silicon layer was deposited via LPCVD (Tempress Systems) on a 100 mm fused silica wafer with 500  $\mu\text{m}$  thickness (Schott Lithotech) directly after cleaning in liquid and fuming nitric acid solutions. A 1.2  $\mu\text{m}$

**Received:** August 24, 2012

**Accepted:** October 29, 2012

**Published:** October 29, 2012

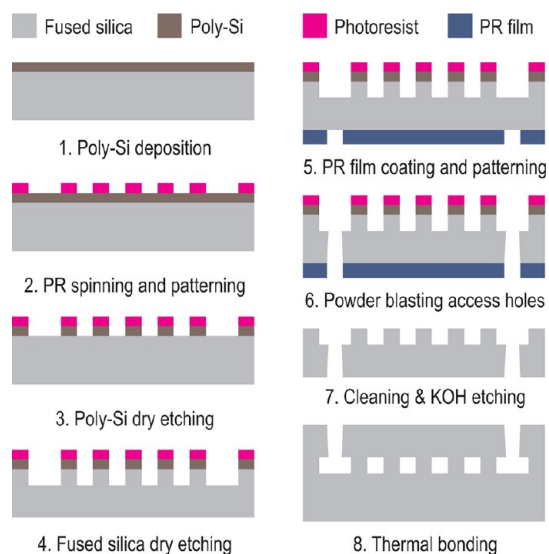


**Figure 1.** Fabrication process flow for fused silica microchips.

thick photoresist (Olin 907-12) layer was spin-coated at 4000 rpm followed by UV-photolithography for transferring the channel layout. The poly-Si layer was etched through by DRIE (Adixen AMS100SE). The patterned poly-Si layer was used as a hard mask for etching fused silica by another DRIE step (Adixen AMS100DE). Subsequently, a thick photoresist film (Ordyl BF410) was laminated on the backside of the wafer and patterned with UV-photolithography. The film served as a mask for through etching of the wafer to open the access holes for the fluidic connections, via powder blasting (with  $29\ \mu\text{m}$  alumina particles), using an in-house built setup. After powder blasting, the wafer was first washed with DI water and then immersed in acetone and isopropanol, respectively. The poly-Si layer was stripped in KOH solution after a cleaning cycle in nitric acid. Next, a bare fused silica wafer was cleaned with the

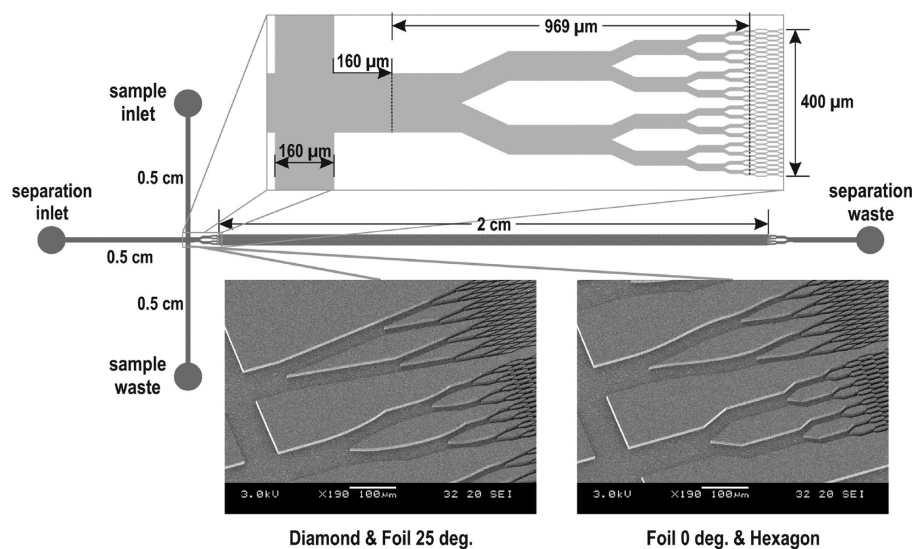
same procedure and directly bonded with the processed wafer in order to obtain closed channels. The bonded stack was kept in a high temperature furnace for the permanent bond for 36 h with ramping up to a maximum temperature of  $1080\ ^\circ\text{C}$  and cooling down back to room temperature with specified rates. As a final step, the stack was diced and individual microchips were fabricated successfully (Figures 2 and 3).

**Microchip Design and Layout.** As mentioned in the introductory part of the paper, the same design configurations as in the previously published theoretical work<sup>12</sup> were evaluated in this experimental study. A unit cell, which was extracted from an infinitely long and wide microchannel, was selected as the domain of interest in the previous study. The reason was to have the ability to make a fair comparison by setting all the critical design parameters, other than geometry definitions, the same. The designs to be evaluated were diamond and hexagons as the known basic geometric shapes and foils with two different tip angles as the newly proposed shapes. Keeping the same unit cell definition, Table 1 summarizes the varied geometrical properties.

For a fair comparison, the same chip design was implemented for all shape alternatives, including a simple cross injector with bifurcating distributor structures, see Figure 2.

**Chemicals.** Buffer solutions were prepared by diluting 20 mM sodium tetraborate stock solutions with deionized water and mixing with acetonitrile (ACN), yielding 10 mM sodium tetraborate buffers with 50% ACN composition. The coumarin dyes (C440, C460, C480, C540) were dissolved in HPLC-grade methanol in order to prepare sample stock solutions that will be diluted while dispensing into the reservoirs during the experiments. All the required chemicals were purchased from Sigma-Aldrich (Zwijndrecht, The Netherlands).

**Chip Coating Procedure.** Inner surfaces of the microchannels were coated with hydrophobic C18 monolayers in order to enable measurements under chromatographic retentive





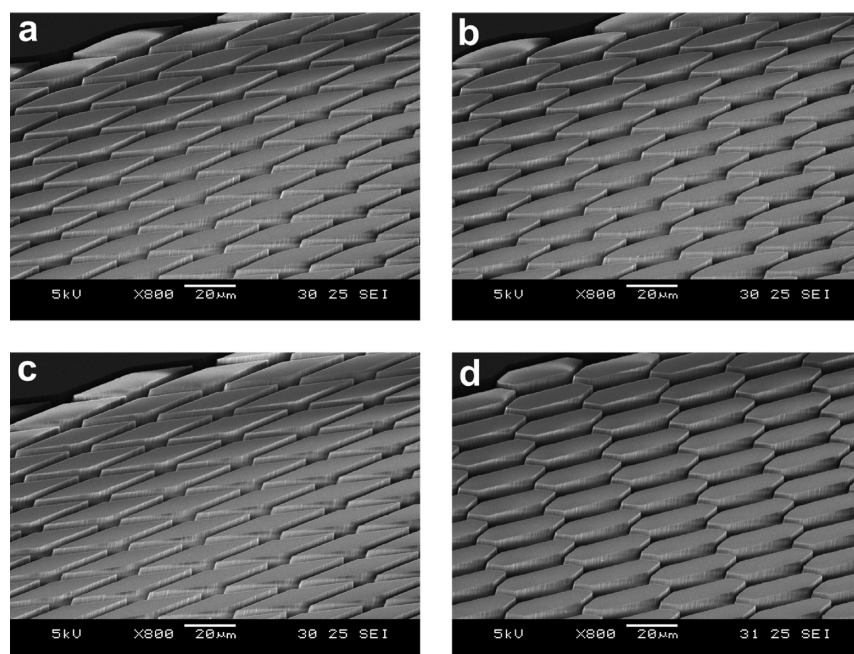


**Figure 2.** Common design of the microchips. To inject a sample, a simple cross layout was implemented, connected to a distributor structure placed  $160\ \mu\text{m}$  downstream of the injection cross. The  $160\ \mu\text{m}$  wide main channel was split into 32 equally wide channels by splitting the channels at half their width at each of the 5 branching steps. Column length was set to 2 cm by placing a collector, which was the mirror image of the distributor, at the end of the column. The total separation channel length was 3 cm wherein 32 and 320 structures were placed in axial and longitudinal directions, respectively. The bottom row represents scanning electron microscopy (SEM) pictures of the distributor structures taken from microchips with the same design. The drawing only shows a hexagonal pillar layout example for simplicity.



**Figure 3.** SEM pictures of fabricated column structures. (a) Foil 0° tip angle, (b) foil 25° tip angle, (c) diamond 16° tip angle, and (d) hexagon 50° tip angle.

**Table 1. Design Parameters of Column Geometries Evaluated in This Study<sup>a</sup>**

				
Pillar length	58.6 $\mu\text{m}$	45.4 $\mu\text{m}$	57.8 $\mu\text{m}$	39.3 $\mu\text{m}$
Pillar width	7.5 $\mu\text{m}$	7.5 $\mu\text{m}$	8.1 $\mu\text{m}$	7.5 $\mu\text{m}$
Wetted perimeter	236.7 $\mu\text{m}$	185.0 $\mu\text{m}$	233.3 $\mu\text{m}$	39.3 $\mu\text{m}$
Minimum spacing	2.37 $\mu\text{m}$	1.95 $\mu\text{m}$	2.17 $\mu\text{m}$	2.27 $\mu\text{m}$
pillar length	58.6 $\mu\text{m}$	45.4 $\mu\text{m}$	57.8 $\mu\text{m}$	39.3 $\mu\text{m}$
pillar width	7.5 $\mu\text{m}$	7.5 $\mu\text{m}$	8.1 $\mu\text{m}$	7.5 $\mu\text{m}$
wetted perimeter	236.7 $\mu\text{m}$	185.0 $\mu\text{m}$	233.3 $\mu\text{m}$	39.3 $\mu\text{m}$
minimum spacing	2.37 $\mu\text{m}$	1.95 $\mu\text{m}$	2.17 $\mu\text{m}$	2.27 $\mu\text{m}$

<sup>a</sup>From left to right: Foil 0° tip angle, foil 25° tip angle, diamond 16° tip angle, and hexagon 50° tip angle. Common parameters are unit cell length of 62.5  $\mu\text{m}$ , unit cell width of 12.5  $\mu\text{m}$ , external porosity of 0.4, and channel depth of 10  $\mu\text{m}$ .

conditions. The applied procedure for coating was based on the one described by Kutter.<sup>13</sup> Since the microchips were fabricated in a cleanroom environment and kept sealed until the moment of starting the experiments, no additional cleaning was applied before the coating process. CNC-machined aluminum holders were used for interfacing the microchip inlet/outlets with the homemade coating setup. Prepared solutions were flushed using Harvard Apparatus PHD 2000 syringe pumps (VWR International BV, Roden, The Netherlands) with Hamilton gastight glass syringes (VWR) through 150  $\mu\text{m}$  inner diameter fused silica tubing from Upchurch Scientific (VWR). In order to have leak-free connections of tubing to the microchips, Upchurch nanoport connectors (VWR) were screwed and tightened through the holes of the holder. First, the microchips were flushed with HPLC-grade methanol with a flow rate of 1  $\mu\text{L}/\text{min}$  for 3 h. Then, toluene (Sigma–Aldrich), which was dried over a 3 Å molecular sieve (Sigma–Aldrich) overnight, was pumped for 5 h with a flow rate of 0.5  $\mu\text{L}/\text{min}$ . Subsequently, the coating solution was passed through with a flow rate of 0.2  $\mu\text{L}/\text{min}$  for a duration of 12 h. The solution was prepared by mixing octadecyltrimethoxysilane (Sigma–Aldrich)

with dry toluene in a 10:90 volumetric ratio. Right before flushing, 5  $\mu\text{L}$  of triethylamine was added as a catalyst for every 1 mL of prepared solution. As the last two steps, toluene was pumped for 5 h at 0.3  $\mu\text{L}/\text{min}$ , and methanol was pumped for 3 h at 0.5  $\mu\text{L}/\text{min}$ . Solutions were flushed continuously through the separation waste channel of the microchips, and excessive solvents were collected from other reservoirs into plastic containers, which were disposed after every run.

**Experimental Procedure.** Microchips were placed in a CNC-machined plastic (acetal copolymer) holder, which allows both interfacing the Nanoport connections for liquid pumping and having around 200  $\mu\text{L}$  reservoirs sealed on top of each inlet/outlet opening. First, methanol was flushed for 10 min with a flow rate of 10  $\mu\text{L}/\text{min}$  through the microchannels in order to wet the entire internal surface. Then, sodium tetraborate buffer (pH 9, 10 mM concentration with 50:50 ACN volumetric composition) was pumped with a flow rate of 5  $\mu\text{L}/\text{min}$  for 20 min. Switching between methanol and buffer streams was accomplished via a manual valve. Considering that the total internal volume of the microchips is 64 nL, pumping 100  $\mu\text{L}$  ensures that methanol is completely replaced with the buffer. After having the microchannels loaded, all the reservoirs were also filled with the buffer solution. Then, 10  $\mu\text{L}$  of 10 mM C480 solution was dispensed into the sample inlet reservoir, which yielded a dilution to 5%. Subsequently, platinum wires, which serve as the electrodes, were immersed inside the reservoirs. The voltages were applied with an eight channel high voltage power supply (Labsmith HVS448-6000D, Mengel Engineering, Virum, Denmark). Injection was performed by applying a 900 V/cm electric field through the injection channel with pinching.<sup>14</sup> Then, the accumulated sample at the injection cross was directed into the separation channel by applying electric fields varying from 0.1 to 1 kV/cm. The same procedure was applied for both coated and uncoated devices (Table 2).

**Detection and Data Processing.** Fluorescence spectroscopy was implemented as a detection method. A Leica

**Table 2.** Applied Electric Potentials at the Reservoirs for the Injection and the Separation

	sample inlet	sample outlet	separation inlet	separation outlet
injection	900 V	0 V	600 V	600 V
separation	0 V	0 V	300–3000 V	0 V

DMI5000 M inverted microscope system (Leica Microsystems, Rijswijk, The Netherlands), which has an integrated motorized stage with electronic position control, was used for the experiments. As a light source, a Leica EL6000 unit, equipped with a mercury short-arc lamp (Osram HXP-R120W/45C VIS, Leica Microsystems), was applied. Fluorescent emission from the sample was passed through a Leica filter cube: D, which consists of an excitation filter (band-pass 355–425 nm), a dichromatic mirror (455 nm), and a suppression filter (long-pass 470 nm). The experiments were monitored using a Leica DFC300FX color camera attached to the microscope. Sample peaks were recorded at positions every 5 mm of the separation channel starting from the point of injection. Resulting movie files were first decomposed into image sequences via VirtualDub (open source software); then, the concentration profiles were plotted with ImageJ (open source) by image processing. As a last step before the calculations, the plotted peaks were fitted as a Gaussian profile, and the variances together with the residence times were directly extracted using OriginPro 8 software (Origin Lab Corporation, USA).

## RESULTS AND DISCUSSION

**Nonretained Species Experiments.** This set of experiments was performed with bare fused silica microchips without any surface treatment (i.e., no stationary phase), which ensures an operation in nonretentive conditions. The concentration profile of the fluorescent dye C480 was monitored as described in the previous section. The presence of this neutral dye at the applied low concentration of around 0.1 mM caused no disturbance in the electric field distribution in the channel. Consequently, the migration of the corresponding zone of this dye expresses the mobile phase velocity at the applied electric fields. One of the key parameters to characterize an electrokinetic system is *mobility*. Therefore, the first parameter to be discussed as a performance measure for the different column geometries is the obtained velocity at a fixed voltage. Figure 4 shows the variation of the mobile phase velocity with respect to the applied electric field. The relationship between these two parameters was linear, as expected, except for the high velocity region, where the mobility curve slightly deviated from linearity when the potential drop exceeded 2 kV. This deviation can most likely be explained by a joule heating effect caused by power dissipation throughout the channel at higher electric currents. This causes an increase in the temperature, therewith an increase in diffusion coefficient and mobility, which is directly related to it.<sup>15,16</sup> In the following plate height analysis, the effect of joule heating on radial diffusion was neglected. For the electric field of 733 V/cm, the measured mobile phase velocities were 1.25, 1.15, 1.14, and 1.06 mm/s for foil with 0°, foil with 25°, hexagon, and diamond, respectively. These values of the electro-osmotic flow (EOF) velocity, generated without surface treatment of the inner walls of the fused silica channels, are high enough for performing CEC experiments close to the optimal velocity for chromatographic separations (see below).

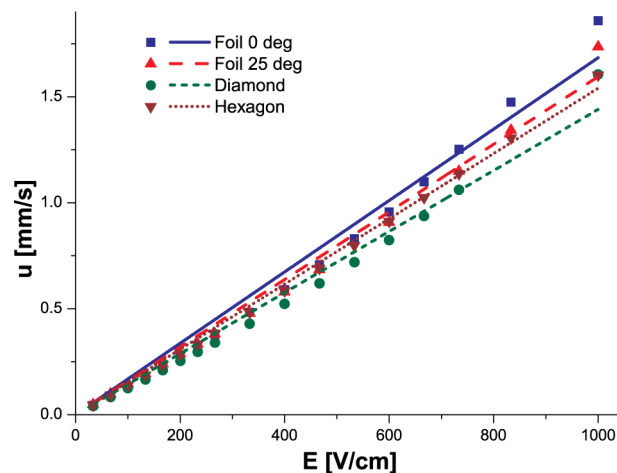


**Figure 4.** Variation of the mobile phase velocity with applied electric field. A linear curve fit intercepting at (0, 0) was implemented. Measured values of the electro-osmotic mobility, which is the slope of the fitted curves, are  $1.68 \times 10^{-8} \text{ m}^2/(\text{V s})$  for foil with 0° tip angle,  $1.60 \times 10^{-8} \text{ m}^2/(\text{V s})$  for foil with 25° tip angle,  $1.54 \times 10^{-8} \text{ m}^2/(\text{V s})$  for hexagon, and  $1.44 \times 10^{-8} \text{ m}^2/(\text{V s})$  for diamond.

One of the design rules for the microchips was minimizing the variation in the total cross section throughout the channels, since such a variation gives a nonuniform axial velocity distribution and therewith additional zone dispersion. As a result, the simulated linear velocities of the mobile phase for all design alternatives were the same and exhibited only a 1% decrease compared to an empty channel.<sup>12</sup> However, experimental measurements resulted in a higher decrease in mean flow velocities, for example, a 5% decrease for the foil with 0° and 20% for diamond, with respect to the empty channel. Being a streamlined body, optimized for minimizing the disturbances through the flow field in the axial direction, the foil shape with 0° tip angle yielded the highest mobility. Increasing the tip angle in the same geometry definition still produces higher velocities when compared with the other alternatives. These results prove that using such optimized structures minimizes the guidance of the electric field and hence the flow field to lateral directions, consequently enabling higher velocity components in the axial direction. In order to check the reliability of the measurements, the monitored velocities at different points in the separation channels were compared. The variances in the measured values were always within a 2% window, which proves the reliability of the data. The other important parameter for evaluating the performance of the columns is *band broadening*. In order to investigate the occurrence of this phenomenon for the studied designs and also enable the possibility of assessing the CEC performance of such systems, theoretical plate heights were determined by the following formula:<sup>17</sup>

$$H_{ji} = \frac{\sigma_j^2 - \sigma_i^2}{(t_{R,j} - t_{R,i})^2} L_{ji} \quad (1)$$

where  $H_{ji}$  is the theoretical plate height determined between the interfaces  $i$  and  $j$ ,  $\sigma^2$  is the peak variance,  $t_R$  is the retention time, and  $L_{ji}$  is the distance between the interfaces  $i$  and  $j$ . Figure 5 illustrates the plate height dependency on mobile phase velocity for the nonretained case. As expected, data sets for each shape alternative yielded close values. Since setting a fixed domain size and external porosity limited the number of

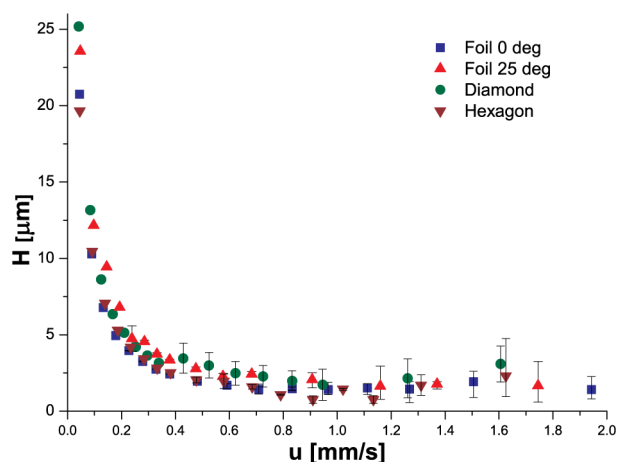


**Figure 5.** Plate height vs mobile phase velocity for the nonretained case.

independent parameters for geometry definitions, the differences in shapes did not result in a significant effect on the performance for such high aspect ratio (length/width) structures for the nonretained case, which is in agreement with our previous modeling study.<sup>12</sup>

After calculating the plate height values for different mobile phase velocities, the results were fitted with the van Deemter equation,<sup>18</sup> which relates the plate height with the mobile phase velocity as follows:

$$h = A + B/v + Cv \quad (2)$$

where  $h$  and  $v$  are the reduced plate height and the linear velocity, respectively. These parameters are rendered dimensionless using the following:<sup>19</sup>

$$h = \frac{H}{d_{\text{eq}}} \quad (3)$$

$$v = \frac{u_0 d_{\text{eq}}}{D_m} \quad (4)$$

where  $D_m$  is the axial diffusion coefficient and  $d_{\text{eq}}$  is the equivalent diameter, which is defined as follows:

$$d_{\text{eq}} = \sqrt{\frac{4A_p}{\pi}} \quad (5)$$

where  $A_p$  is the cross-sectional area of the pillar in the  $xy$  plane, which coincides with the flow direction. The  $A$ ,  $B$ , and  $C$  terms are assumed to be constants, where the  $A$  term represents eddy diffusion, the  $B$  term represents longitudinal diffusion, and the  $C$  term represents resistance to mass transfer.

As can be concluded from eq 5,  $d_{\text{eq}}$  is defined as the diameter of a circular pillar with the same area in the  $xy$  plane.<sup>20</sup> Since in conventional CEC applications columns are packed with spherical particles, their diameters are used as a reduction parameter. In order to compare the performance of microfabricated columns having custom shapes with conventional systems or with other microsystems with different column geometries, the equivalent diameter definition was selected. Alternatively, domain size (since unit cells were defined as building blocks of the column) or minimum channel spacing on the plane, which is perpendicular to the flow direction, may be defined as a reduction parameter.<sup>20</sup> Since it is not possible to

assess the relative validity or accuracy of these reduction parameters, the external porosity, the unit cell size, and the interpillar spacing in the lateral direction were kept constant for all the geometry alternatives. Figure 6 illustrates the fitted van

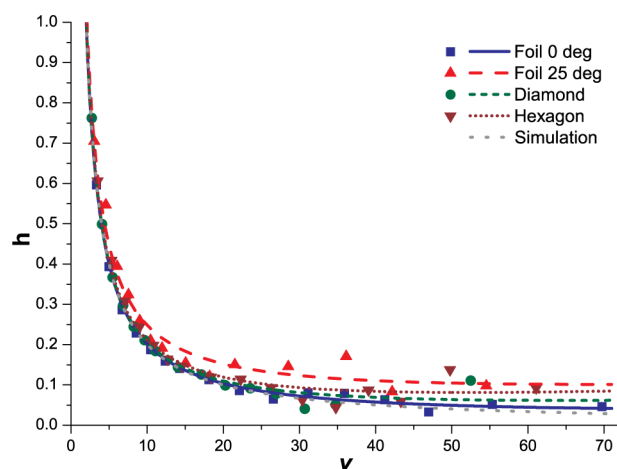


**Figure 6.** Plate height vs velocity for reduced parameters for the nonretained case. Experimental results for different shapes are also compared with the simulations. The span of the  $x$  axis (reduced velocity) is limited to the experimental working range. The simulation curve represents the data for all geometries.

Deemter curves for reduced parameters, using the equivalent cylindrical pillar diameter as a reduction parameter. Simulation data was also represented as a single curve, as the variations of the fitted constants were negligible for different shapes. The foil shape with  $0^\circ$  angle yielded the lowest plate height values, with a slight deviation from the simulation results, while the  $25^\circ$  alternative showed a similar trend with a shift upward. Diamond and hexagon shapes produced curves between that of the respective foil shapes, while the latter resulted in a higher performance.

In order to be able to discuss the physical meaning of the results in more detail and compare the characteristics of the designs in all aspects, the constants of the fitted van Deemter curves are summarized in Table 3.

**Table 3.**  $A$ ,  $B$ , and  $C$  Terms of the Fitted van Deemter Curves for the Studied Design Alternatives<sup>a</sup>

	foil $0^\circ$	foil $25^\circ$	diamond	hexagon	simulation
$A$	0.00000	0.04389	0.00000	0.00463	0.00000
$B$	1.99623	2.00016	2.00062	2.00024	2.00000
$C$	0.00019	0.00041	0.00047	0.00073	0.00000

<sup>a</sup> $R^2$  and reduced  $\chi^2$  values were 0.999 and 0.0001, 0.990 and 0.0010, 0.997 and 0.0004, and 0.991 and 0.0006 for foil  $0^\circ$ , foil  $25^\circ$ , diamond, and hexagon, respectively.

Since the  $A$  term depends on the channel geometry, in other words the randomness of the flow paths of the migrating species, higher aspect ratio structures produced better results. As shown in Table 1, the foil with  $0^\circ$  and the diamond structures had a much higher aspect ratio (length over width) than the other two. Comparing the pillar lengths with the unit cell length, the  $0^\circ$  foil and the diamond structures yielded merging and splitting microchannels with small coupling zones, where the  $25^\circ$  foil and the hexagon structures produced wide and narrow microchannels coupled one after another in an

alternating pattern. As a result, the  $0^\circ$  foil and diamond structures had no contribution to the plate height, since they do not provide propagation of eddy diffusion. The  $A$  term for the hexagon structure was 1 order of magnitude smaller than that for the  $25^\circ$  foil, because of its straight microchannels in the longitudinal direction, where the  $25^\circ$  foil structure had a much higher radius of curvature as a source of dispersion. The hexagon structure yielded the lowest effective diffusion coefficient, since it was the only alternative that gave the ability to preserve the constant cross section along the channel. Therefore, the fluctuations in the flow field (increasing/decreasing mean flow velocity during migration) in this case are minimized. Although it was not possible to keep the cross section constant with a foil shape, the  $0^\circ$  alternative resulted in only 2% increase, because of its optimized geometry and placement definition.<sup>12</sup> The  $B$  term, as expected, is very close to 2 and is virtually the same for all the alternative designs. With the absence of retention, the  $C$  term strongly depends on the column design. Therefore, the foils, which are streamlined, hydrodynamically optimized structures and also placed with the rule of preserving the hydrodynamic balance, produced much better results compared to diamond and hexagon structures.

**Retained Species Experiments.** These experiments were performed with the C18-coated channels to realize retained conditions. C480 was again monitored to characterize the microchannels. Only two variants among the four were selected for this study. The foil with  $0^\circ$  was the best candidate according to the nonretained measurements, while the one with  $25^\circ$  was the worst. For that reason, the latter was eliminated. Since the performance of the diamond shape was better than that of the hexagon shape, the latter was eliminated, also because it produces a much lower wetted surface (Table 1), which is directly proportional to the retention coefficient and therefore should be as large as possible, considering the nonporous nature of the structures. Furthermore, it was shown in our previous theoretical study<sup>12</sup> that a foil with  $0^\circ$  tip angle and the diamond design were the best two alternatives. Figure 7 shows the measured plate heights at different mobile phase velocities. For practical reasons, the calculated velocities of C440 as the least retained compound were taken as the corresponding mobile phase velocities. The lowest plate height values were around 2.3 and 3.5  $\mu\text{m}$  for foil and diamond, respectively. In our modeling study, the foil shape yielded moderately lower

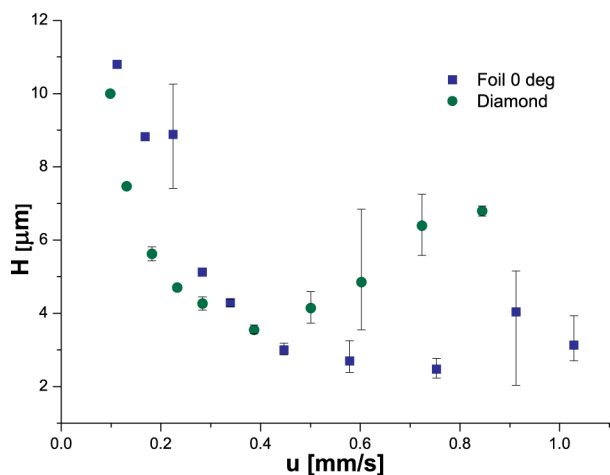


**Figure 7.** Plate height for the dye C480 vs mobile phase velocity for the retained case.

plate heights than the diamond structure; however, the experimental results show that the foil shape has a significantly better performance than the diamond design.

Unlike in the nonretained case, the van Deemter equation was inadequate for producing a proper fit for the retained experiments. The  $A$  terms, which were absent in the nonretained measurements, turned out to be negative in order to have a proper fit for eq 2. This finding does not make sense physically: a negative  $A$  term represents an antidispersive mechanism, which instead of to broaden, would cause the peak to shrink. The only known peak compression effect for liquid separation methods is electrokinetic stacking,<sup>21</sup> which generally is asymmetric, while here we observe symmetric Gaussian peaks. There is no reason to assume that stacking would have occurred in our experiments. Furthermore, by definition, the  $A$  term is a measure of disorder within the flow path, which cannot be less than nonexistent. In other words, the ideal condition, yielding a zero  $A$  term, is a perfectly straight path line for each individual molecule migrating through the column.

In order to find an explanation, a literature search was performed, from which it was found that a negative  $A$  term is sometimes observed in gas chromatography (GC)<sup>22</sup> and the possible reasons for such a phenomenon were either compression of the gaseous species or local variations in coating quality. To compensate for these effects, the exit velocity of the system was taken as the mobile phase velocity, and with that, the  $A$  term became positive. Since compressibility is out of the question for LC and the applied measurement technique in this study is completely different from that in GC applications, this provides no satisfactory explanation for the occurrence of the negative  $A$  term in our work. Furthermore, in our case, the liquid velocity at every 5 mm of the separation channel was measured to check whether the linear velocity decreases along the channel while sample migrates toward the outlet. A negligible change was found indicating that the migration velocity of the peaks was almost constant. The velocities at control points were not measured directly but calculated with respect to the migration time of the sample from one node to another, which in principle gives mean velocities. Having these mean velocities at every 5 mm interfaces unchanged along the channel eliminates the necessity of a direct measurement of the exit velocity. Kutter and co-workers reported an open channel microchip CEC application<sup>13</sup> with a coumarin dye mixture for the same hydrophobic coating as was applied in this study. They provided a plate height versus linear velocity plot for C460 for three different channel depths, which includes both measured data points and a fitted van Deemter curve, but they did not report the resulting constants of the used fitting equation. We have extracted the experimental data from their figure and fitted them with eq 2 with a positive  $A$  term limitation and replotted with the same axes scales. The reproduced curve with a non-negative  $A$  term restriction failed to converge to Kutter's original plot. Following the same fitting procedure for the data of Regnier and co-workers, who reported a modeling study on open channel CEC,<sup>23</sup> again it was found that fitting was not successful with a non-negative  $A$  term. Since the work of Regnier as discussed above was a modeling study, improper coating may be ruled out as an explanation for improper fitting. Similar trends for the  $A$  term were also observed for conventional HPLC applications.<sup>24,25</sup> It was concluded that setting the  $A$  term as a velocity-independent constant was an oversimplification, which caused a loss of data for defining the relationship between the plate

height and the mobile phase velocity. As described by Knox,<sup>26,27</sup> the  $A$  term was selected as a parameter that changes with the linear velocity. Being the most comprehensive option, the Knox and Parcher equation<sup>28</sup> was selected as a starting point for revealing the relationship. However, the constant  $A$  term was eliminated since the  $A$  terms of the van Deemter fits for the nonretained case were also missing. Therefore, the used equation for fitting the data of the retained experiments was a generalized Knox equation:<sup>27</sup>

$$h = Av^n + B/v + C_s v \quad (6)$$

where  $n$  is the power of the linear velocity, which is a constant parameter. In addition to its characteristics mentioned in the previous section, the  $A$  term also includes the effects of dispersive mechanisms in the mobile phase including retention, where the  $C_s$  term defines the effect of retention in the stationary phase. Figure 8 illustrates the fitted curves for the reduced parameters. The parameters of the generalized Knox equation fitted to the experimental data are summarized in Table 4.

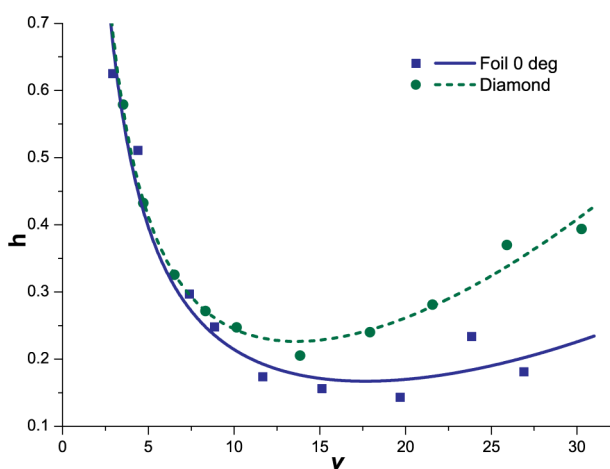


**Figure 8.** Plate height vs velocity for reduced parameters for the retained case.

**Table 4.** Coefficients of the Fitted Generalized Knox Equations for Foil and Diamond under Retentive Conditions<sup>a</sup>

	foil 0°	diamond
$A$	0.00019	0.00064
$B$	1.96244	1.99857
$C_s$	0.00000	0.00000
$n$	1.98463	1.84453

<sup>a</sup> $R^2$  and reduced  $\chi^2$  values were 0.939 and 0.0018 and 0.978 and 0.0003 for foil 0° and diamond, respectively.

Having  $R^2$  values larger than 0.94, the generalized Knox equation produced better fits. It was also shown previously<sup>28</sup> that this equation provides a good estimate for low reduced velocities ( $30 < v < 300$ ), which was the case in this work. Setting the parameter  $n$  as zero yields the typical van Deemter equation, which appeared to be the best fit for nonretained measurement data.

As a hydrodynamically optimized geometry, the foil shape yielded a much lower  $A$  term than the diamond shape. By using the generalized Knox equation, this term now includes the effects of mass transfer limitations in the mobile phase. In other

common expressions, this contribution is often referred to as the  $C_m$  term.<sup>28</sup> The obtained  $B$  term had again a similar value as in the other cases, which was observed after reduction using the same parameters as described above. This is expected as it represents the diffusion of the sample in the mobile phase, where the same dye and buffer were used for all the experiments. The  $C_s$  term, which represents the mass transfer resistance in the stationary phase, was absent using the generalized Knox equation. The channel walls were coated with monolayers as described previously; therefore, there was no solute transport within the stationary phase, which yielded no contribution for the  $C$  term in this equation. For a more comprehensive study, more data points containing several combinations of mobile phase composition and concomitant retention factors would be needed, especially in the  $C$  term region. For this specific requirement, shorter channels should be fabricated to avoid resistive heating at these high velocity data points. This is beyond the scope of the current paper but will be treated in a future study.

**Kinetic Plots.** The quality of a packing is determined by both the theoretical plate height values and the electroosmotic mobility. To allow for a direct interpretation of the combined values, an analogue of the kinetic plot method<sup>29</sup> in pressure driven mode can be constructed for electrically driven separations. First, the number of plates and the analysis time are defined as follows:

$$N = \Delta V \left[ \frac{\mu_0}{u_0 H} \right]_{\text{exp}} \quad (7)$$

$$t_0 = \Delta V \left[ \frac{\mu_0}{u_0^2} \right]_{\text{exp}} \quad (8)$$

where  $\Delta V$  is the differential electric potential applied throughout the channel,  $\mu_0$  is the measured electro-osmotic mobility,  $u_0$  is the measured linear velocity, and  $H$  is the calculated plate height. Figure 9 represents the kinetic performance of the analyzed structures for the nonretained case for a 6 kV voltage drop. The superior permeability and

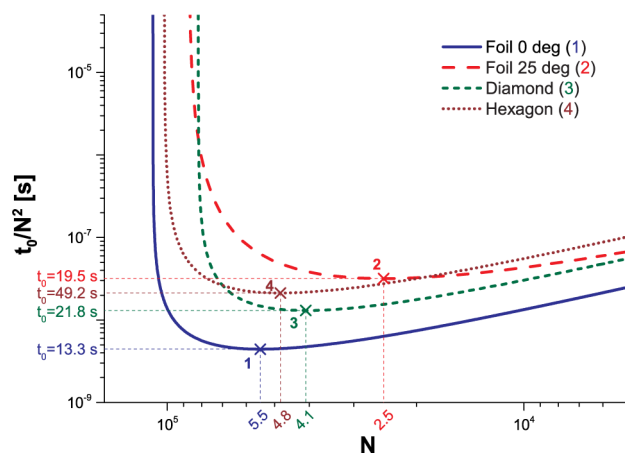


**Figure 9.** Kinetic plot representation of the relationship between the analysis time and the produced number of plates. (x) represents the optimum working points for each alternative. 1:  $N_{\text{opt}} = 54\,824$ ,  $t_0 = 13.33$  s,  $L = 3.67$  cm; 2:  $N_{\text{opt}} = 24\,737$ ,  $t_0 = 19.48$  s,  $L = 4.32$  cm; 3:  $N_{\text{opt}} = 40\,890$ ,  $t_0 = 21.82$  s,  $L = 4.34$  cm; 4:  $N_{\text{opt}} = 48\,121$ ,  $t_0 = 49.23$  s,  $L = 6.75$  cm. Applied voltage drop was 6 kV.

plate count of the foil shape with  $0^\circ$  angle is clearly reflected in Figure 9, as the time to generate  $N$  plates is the lowest for all considered  $N$  values. This is in contrast with typical kinetic plots based on pressure propulsion comparing different features with identical porosities,<sup>29</sup> where in a uniformly packed configuration, improved plate heights occur at the expense of larger pressure drops. The length that is required to operate the foil shape with  $0^\circ$  angle under nonretained conditions at the kinetically most favorable condition is 3.67 cm, which corresponds to 54 800 plates that are generated in a time frame of 13 s only.

It is of course more relevant to represent the kinetic performance under retained conditions, expressing the number of plates now in effective number of plates  $N_{\text{eff}}$ . The following expressions describe the kinetic performance under retained conditions:

$$N_{\text{eff}} = N \frac{k^2}{(1+k)^2} \quad (9)$$

$$t_{\text{R}} = t_0(1+k) \quad (10)$$

where  $k$  is the retention factor,  $t_{\text{R}}$  is the retained elution time, and  $t_0$  the void time. Figure 10 represents the kinetic

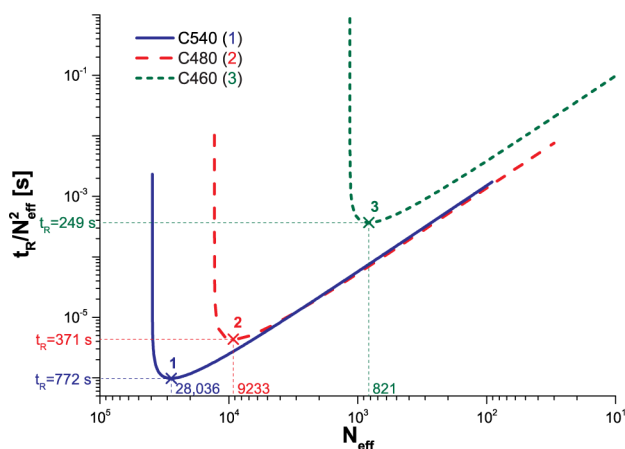


**Figure 10.** Kinetic plot representation of the separation performance of the foil shape with  $0^\circ$  for C460, C480, and C540, respectively. (x) represents the optimum working points for each alternative. 1:  $N_{\text{eff}} = 28\,036$ ,  $t_{\text{R}} = 772$  s; 2:  $N_{\text{eff}} = 9233$ ,  $t_{\text{R}} = 371$  s; 3:  $N_{\text{eff}} = 821$ ,  $t_{\text{R}} = 249$  s. Applied voltage drop was 6 kV. Optimum channel length was 14.8 cm for all cases.

performance of the proposed foil shape with  $0^\circ$  tip angle for the monitored fluorescent dyes. For a retained component with a relatively large retention coefficient (given the nonporous nature of the pillars) of  $k = 2.54$ , a channel length of 14.8 cm would be required to generate the highest number of plates per unit of time, that is,  $N_{\text{eff}} = 28\,036$  in about 13 min.

**Separation Experiment.** With the aim of finding the optimized column design for CEC, a separation experiment of four coumarin dyes (C440, C460, C480, and C540) was performed. Figure 11 illustrates the separated three bands: C460, C480, and C540 at 5 mm downstream of the injection point. Although its separation from the injected plug could be monitored within the first 300  $\mu\text{m}$ , it was not possible to distinguish the C440 signal from the background noise at the detection point, due to limited camera sensitivity. Separation of all dyes was achieved in less than 25 s with very high resolution,

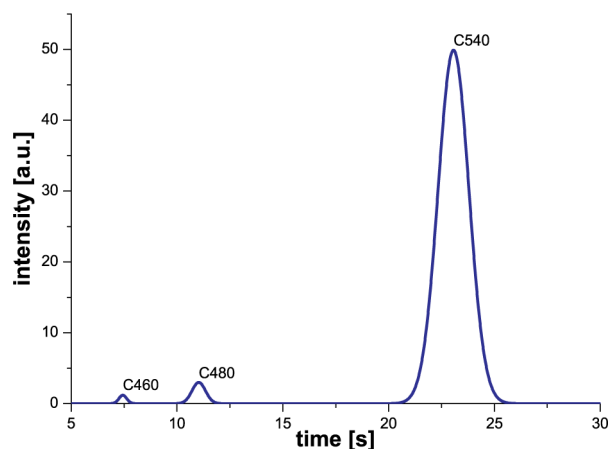


**Figure 11.** Three coumarin dyes (C460, C480, and C540) separated at 500 V/cm ( $L_{\text{sep}} = 5$  mm;  $u_0 = 0.77$  mm/s). Stationary phase: octadecyltrimethoxysilane; mobile phase: 10 mM sodium tetraborate (pH 9) with 50:50 ACN volumetric ratio. Horizontal axis represents elapsed time after injection. Measured retention factors:  $k_{\text{C460}} = 0.14$ ,  $k_{\text{C480}} = 0.7$ , and  $k_{\text{C540}} = 2.54$ . Measured resolutions:  $R_{\text{C480-C460}} = 7.14$ ;  $R_{\text{C540-C480}} = 11.5$ .

which confirms that baseline resolution can easily be reached at very short separation lengths, hence within a very short time of operation.

## CONCLUDING REMARKS

Experimental validation of the previously reported design and optimization method was performed, and it was confirmed that the performance of the microfabricated column structures can be maximized by the newly proposed foil definition. More specifically, it was possible to reach 1.8 million plates per meter for the nonretained mode and 540 000 for an analyte with a retention factor of  $k = 0.86$  without any further optimization for side-wall effects or channel depth (which was fixed at 10  $\mu\text{m}$ ). Moreover, the lowest reduced plate height was around 0.06 for nonretained runs at the optimum working potential.

## AUTHOR INFORMATION

### Corresponding Author

\*E-mail: j.g.e.gardeniers@utwente.nl; fax: +31 (0)53 4894683.

### Notes

The authors declare no competing financial interest.

## ACKNOWLEDGMENTS

This work was financially supported by IWT-Flanders within the NextChrom project.

## REFERENCES

- (1) He, B.; Tait, N.; Regnier, F. *Anal. Chem.* **1998**, *70*, 3790–3797.
- (2) Regnier, F. *J. High Resolut. Chromatogr.* **2000**, *23*, 19–26.
- (3) Slentz, B. E.; Penner, N. A.; Regnier, F. *J. Sep. Sci.* **2002**, *25*, 1011–1018.
- (4) Mogensen, K. B.; Eriksson, F.; Gustafsson, O.; Nikolajsen, R. P. H.; Kutter, J. P. *Electrophoresis* **2004**, *25*, 3788–3795.
- (5) Gustafsson, O.; Mogensen, K. B.; Kutter, J. P. *Electrophoresis* **2008**, *29*, 3145–3152.
- (6) Kirchner, J.; Hasselbrink, E., Jr. *Anal. Chem.* **2005**, *77*, 1140–1146.
- (7) Gzil, P.; Vervoort, N.; Baron, G.; Desmet, G. *Anal. Chem.* **2003**, *75*, 6244–6250.



- (8) De Smet, J.; Gzil, P.; Vervoort, N.; Verelst, H.; Baron, G.; Desmet, G. *Anal. Chem.* **2004**, *76*, 3716–3726.
- (9) Billen, J.; Gzil, P.; Vervoort, N.; Baron, G.; Desmet, G. *J. Chromatogr., A* **2005**, *1073*, 53–61.
- (10) De Pra, M.; Kok, W. T.; Gardeniers, J. G. E.; Desmet, G.; Eeltink, S.; van Nieuwkastele, J. W.; Schoenmakers, P. J. *Anal. Chem.* **2006**, *78*, 6519–6525.
- (11) De Pra, M.; De Malsche, W.; Desmet, G.; Schoenmakers, P.; Kok, W. *J. Sep. Sci.* **2007**, *30*, 1453–1460.
- (12) Sukas, S.; Desmet, G.; Gardeniers, H. J. G. E. *Electrophoresis* **2010**, *31*, 3681–3690.
- (13) Kutter, J. P.; Jacobson, S. C.; Matsubara, N.; Ramsey, J. M. *Anal. Chem.* **1998**, *70*, 3291–3297.
- (14) Ermakov, S. V.; Jacobson, S. C.; Ramsey, J. M. *Anal. Chem.* **2000**, *72*, 3512–3517.
- (15) Petersen, N. J.; Nikolajsen, R. P. H.; Mogensen, K. B.; Kutter, J. P. *Electrophoresis* **2004**, *25*, 253–269.
- (16) Rathore, A. S. J. *J. Chromatogr., A* **2004**, *1037*, 431–443.
- (17) Lough, W. J.; Wainer, I. W. *High Performance Liquid Chromatography, Fundamental Principles and Practice*; Blackie Academic & Professional: Glasgow, Scotland, 1996; pp 20–29.
- (18) Van Deemter, J.; Zuiderweg, F.; Klinkenberg, A. *Chem. Eng. Sci.* **1956**, *5*, 271–289.
- (19) Giddings, J. C. *Dynamics of Chromatography, Part 1: Principles and Theory*; Marcel Dekker: New York, 1965; pp 56–60.
- (20) Gzil, P.; De Smet, J.; Vervoort, N.; Verelst, H.; Baron, G. V.; Desmet, G. *J. Chromatogr., A* **2004**, *1030*, 53–62.
- (21) Palmer, J.; Burgi, D. S.; Landers, J. P. *Anal. Chem.* **2002**, *74*, 632–638.
- (22) Svec, F.; Kurganov, A. A. *J. Chromatogr., A* **2008**, *1184*, 281–295.
- (23) Zhang, X.; Regnier, F. E. *J. Chromatogr., A* **2000**, *869*, 319–328.
- (24) Ishizuka, N.; Minakuchi, H.; Nakanishi, K.; Soga, N.; Hosoya, K.; Tanaka, N. *J. High Resolut. Chromatogr.* **1998**, *21*, 477–479.
- (25) Ishizuka, N.; Minakuchi, H.; Nakanishi, K.; Soga, N.; Nagayama, H.; Hosoya, K.; Tanaka, N. *Anal. Chem.* **2000**, *72*, 1275–1280.
- (26) Knox, J. H. *J. Chromatogr., A* **1999**, *831*, 3–15.
- (27) Knox, J. H. *J. Chromatogr., A* **2002**, *960*, 7–18.
- (28) Billen, J.; Gzil, P.; De Smet, J.; Vervoort, N.; Desmet, G. *Anal. Chim. Acta* **2006**, *557*, 11–18.
- (29) Desmet, G.; Clicq, D.; Gzil, P. *Anal. Chem.* **2005**, *77*, 4058–4070.